Građevinski materijali i konstrukcije
Building Materials and Structures
journal homepage: www.buildingmaterialsstructures.com

https://doi.org/10.5937/GRMK2600025S

Original scientific paper

Winkler modeling of surge shafts in rock under vertically propagating shear waves

Branislav Stupar[1)], Nikola Tomić[*2)]

[1)] *Energoprojekt Hidroinženjering, Bulevar Mihajla Pupina 12, 11000, Belgrade, Serbia*
[2)] *Institute for Testing of Materials (IMS Institute), Bulevar vojvode Mišića 43, 11000, Belgrade, Serbia*

Article history
Received: 30 August 2026
Received in revised form:
15 October 2026
Accepted: 21 October 2026
Available online: 04 November 2026

Keywords
hydropower,
underground structures,
vertical shafts,
earthquake,
dynamic,
SSI,
elastic,
analytical

ABSTRACT

This paper presents a closed-form frequency-domain solution for seismic response of vertical shafts in rock, transformed to the time domain by inverse fast Fourier transform (FFT). A deep reinforced-concrete shaft is modeled as a Timoshenko beam on lateral and rotational Winkler springs. The solution is verified against an independent time-domain finite-element analysis by comparing peak envelopes and time histories of the response quantities. Six modeling assumptions are evaluated: beam kinematics, base fixity, lateral and rotational ground reaction, shaft inertia and ground radiation damping. The results indicate that the shaft response is predominantly governed by kinematic compatibility with the displacement field of the surrounding ground. Shaft inertia and kinematic coupling through dashpots increase the peak shear force by only 4.3% and 1.2% respectively, with other response quantities practically unaffected. No resonance occurs for the considered range of input parameters, as the shaft's fundamental frequency stays far above the frequency band containing significant ground-motion energy. Findings of this work indicate that simplified static approaches may be safely used for preliminary design. A set of modeling decisions that ensures upper-bound engineering estimates of design quantities is proposed. The closed-form solution and a benchmark example are provided to facilitate verification of numerical models.

1 Introduction

Surge shafts are hydraulic structures placed between the main storage reservoir and the powerhouse of a hydroelectric power plant (Fig. 1). The surge chamber is intended to absorb sudden rises of pressure, as well as to compensate for brief drops in water supply. They are usually constructed as circular reinforced-concrete-lined shafts embedded in rock. As is the case with other large underground structures, seismic design requires the interaction of the structure and the surrounding ground to be considered.

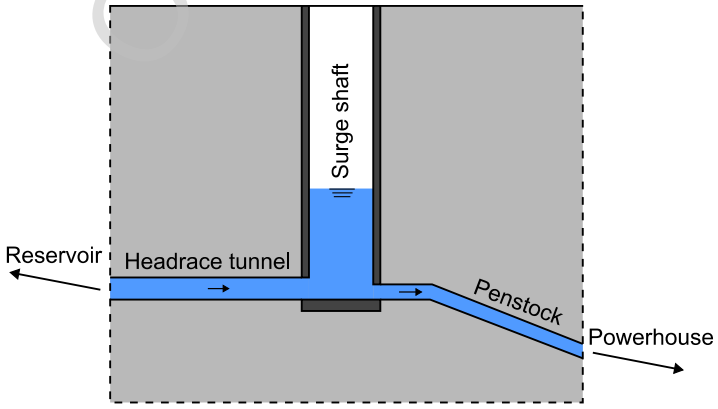


Figure 1. General schematic view of a surge shaft

* Corresponding author:
E-mail address: nikola.tomic@institutims.rs

Seismic response of vertical underground shafts is generally governed by the vertically propagating shear (S) waves. While the S waves cause racking (i.e. cross-section distortion) in tunnels [1,2], the vertically oriented shafts are subjected to longitudinal bending and transverse shear action. Elastic analysis has been traditionally used and is generally considered sufficient due to low-damage design objective and brittle failure modes of rock mass. Complex design scenarios, with multiple soil layers or variable lining cross-section, may warrant a more detailed numerical model and possible consideration of nonlinearity. Lack of usable experimental data, and thus the inability to perform proper model validation, comes as one of the main challenges in modeling of large underground structures. To ensure that the model performs as intended, a verification against reliable baseline results should be conducted before introducing the project-specific complexity.

Neither the well-established Winkler pile models, nor the models for caissons, can be directly used to analyze seismic response of surge shafts. Specific proportions of surge shafts, such as large depth, moderately large diameter and robust lining dimensions clearly invalidate some of the fundamental hypotheses of both pile and caisson analytical models. Due to pile slenderness, Euler-Bernoulli beam kinematics and negligible longitudinal friction at the soil-structure interface (i.e. no rotational compliance) are normally assumed [3]. The family of models developed by Zhang et al. [4,5], intended for slender shafts in soft soil, still retains the fundamental pile model assumptions – Euler-Bernoulli beam formulation and no rotational interaction with the soil. The three-dimensional elastodynamic continuum model, proposed by Yang et al. [6], also retains the two pile-specific assumptions. Rigid-body behavior of the structure, commonly assumed in caisson analysis [7–9], is also inapplicable to surge shafts embedded in rock. Therefore, a new class of models, built upon a set of hypotheses applicable to surge shafts specifically, needs to be developed.

This paper introduces a closed-form analytical solution, specifically developed for seismic analysis of surge shafts in rock. The proposed model incorporates a frequency-domain ground response solution, as well as classical Winkler mechanics, modified to represent the behavior of surge shafts under vertically propagating shear waves more realistically. The Winkler approach was chosen for its simple numerical implementation and future extensibility to nonlinear problems. While it shares the basic concepts with the Winkler model of Zhang et al. [4], the proposed solution introduces several modifications and improvements that were necessary for its application to deep reinforced-concrete shafts in rock:

- Timoshenko beam kinematics are implemented instead of Euler-Bernoulli.
- Base-relative free-field translation is imposed onto the structural model, which is necessary for it to be consistent with the applied fixed-base boundary condition. Lining inertia due to absolute base acceleration is introduced as a separate body force.
- Rotational Winkler springs, derived from an anti-plane shear solution [10], are introduced to account for the longitudinal friction between the shaft lining and the surrounding rock.
- Stiffness of the soil-structure interface is recalibrated following the caisson solution of Gerolymos and Gazetas [8], to take into account the relatively large diameter of the shaft.
- Constant, frequency-independent radiation damping is introduced for consistency with time-domain numerical models.

The proposed analytical model is rigorously verified against an independent numerical model. Python code, implementing both the analytical and the numerical model, is made publicly available [11].

Besides the analytical formulation, this paper also proposes a design-oriented analysis methodology, derived from the parametric study. Objective of the proposed procedure is to obtain safe engineering estimates of the design quantities, while avoiding or mitigating the major modeling uncertainties.

2 Analytical formulation

The closed-form frequency-domain solution is presented in this section. General concept of the model, described further on, is schematically represented in Fig. 2.

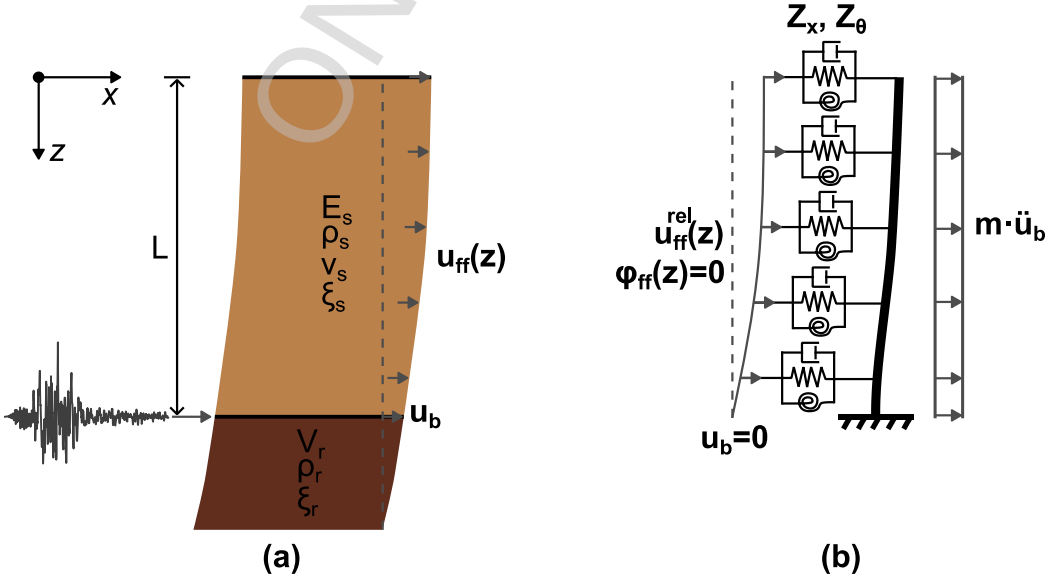


Figure 2. (a) Ground response analysis; (b) Structural model

ONLINE FIRST

2.1 Ground response

Free-field response is evaluated in the frequency domain, employing the conventional one-dimensional ground response analysis [12]. An outcrop motion is applied at the base of a single-layer soil profile, sitting on top of a compliant elastic half-space (Fig. 2a). Acceleration record is zero-padded, band-limited and converted to an acceleration spectrum by FFT. A displacement spectrum is obtained by dividing the acceleration spectrum by $-\omega^2$, where ω denotes circular frequency.

The complex shear modulus of Dormieux and Canou [13], with the layer damping ratio ξ_s written in place of the loss coefficient $\eta = 2\xi$, is written as:

$$G_s^* = G_s\left(\sqrt{1-4\xi_s^2} + 2i\xi_s\right) \tag{1}$$

The complex wave number is:

$$\kappa = \frac{\omega}{V_s\sqrt{G_s^*/G_s}} \tag{2}$$

where $V_s = \sqrt{G_s/\rho_s}$ is the shear wave velocity. The boundary condition of zero shear stress at the surface reduces the displacement profile to a cosine:

$$u_{ff}(z) = U_s \cos \kappa z \tag{3}$$

where U_s is the complex displacement amplitude at the surface. For an outcrop motion U_{out} applied at the layer base, condition of displacement and shear stress continuity at $z = L$ and radiation in the half-space, the complex displacement amplitude at the surface is:

$$U_s = \frac{U_{out}}{\cos \kappa L + i\alpha \sin \kappa L} \tag{4}$$

where α is the complex impedance ratio between the layer and the bedrock below:

$$\alpha = \frac{\rho_s V_s \sqrt{G_s^*/G_s}}{\rho_r V_r \sqrt{G_r^*/G_r}} \tag{5}$$

with subscript r denoting the bedrock.

To ensure consistency with boundary conditions of the structural model, the free-field displacement needs to be corrected so it is base-relative. The base displacement u_b is subtracted from the absolute free-field displacement:

$$u_{ff}^{rel}(z) = u_{ff}(z) - u_b = U_s(\cos \kappa z - \cos \kappa L) \tag{6}$$

The free-field rotation imposed onto the structural model is zero, since horizontal slices of ground do not rotate under shear waves:

$$\varphi_{ff}(z) = 0 \tag{7}$$

2.2 Structural model

Surge shaft is modeled as a Timoshenko beam on Winkler springs, onto which the free-field response is imposed (Fig. 2b). Response quantities of the shaft are denoted as w (displacement), θ (rotation), M (bending moment) and V (shear force).

Damping of the lining material is stiffness-proportional and introduced as a complex rigidity:

$$EI^* = EI(1 + i\omega\beta_K), \qquad GA^* = GA(1 + i\omega\beta_K) \tag{8}$$

with β_K the Rayleigh stiffness coefficient, and effective shear area of the hollow circular section adopted from Cowper [14]. These complex rigidities are used when solving the governing equations, while the section forces are evaluated from the elastic rigidities EI and GA.

The ground is represented by translational and rotational distributed springs, with radiation damping included in the lateral direction:

$$Z_x = k_x + i\omega c_x \tag{9}$$

$$Z_\theta = k_\theta \tag{10}$$

Lateral springs are calibrated following Gerolymos and Gazetas [8], while the rotational springs are derived from anti-plane shear mechanics of a cylindrical boundary in elastic medium [10]:

$$k_x = 1.75(L/d)^{-0.13}E_s, \qquad k_\theta = \pi G_s d^2/4 \tag{11}$$

Lateral dashpot coefficient, based on the high-frequency asymptote from Gazetas and Dobry [15], is:

$$c_x = \frac{\pi}{2}\left(1 + \frac{3.4}{\pi(1-\nu_s)}\right)\rho_s V_s d \tag{12}$$

with index s denoting the soil layer and d the shaft diameter. The governing equations, i.e. the translational and rotational equilibrium, are:

$$GA^*\left(\frac{d^2w}{dz^2} - \frac{d\theta}{dz}\right) + \rho A\omega^2 w - Z_x\left(w - u_{ff}^{rel}\right) + \\ + \rho A\omega^2 u_b = 0 \tag{13}$$

$$EI^*\frac{d^2\theta}{dz^2} + \rho I\omega^2\theta + GA^*\left(\frac{dw}{dz} - \theta\right) - Z_\theta\theta = 0 \tag{14}$$

Note the base-relative translational displacement and added inertial term that accounts for base acceleration in Eq. (13). The section forces of the shaft lining are:

$$M(z) = EI\frac{d\theta}{dz}, \qquad V(z) = -GA\left(\frac{dw}{dz} - \theta\right) \tag{15}$$

Boundary conditions are defined so the top is free and the base is clamped or pinned:

$$M(0) = 0, \qquad V(0) = 0, \qquad w(L) = 0,$$
$$\begin{cases} \theta(L) = 0 \ (fixed) \\ M(L) = 0 \ (pinned) \end{cases} \tag{16}$$

2.3 Closed-form solution

Substituting $w = e^{\lambda z}$ and $\theta = Be^{\lambda z}$ into the homogeneous form of the Eq. (14) gives the rotation-to-displacement ratio:

$$B = -\frac{GA^*\lambda}{EI^*\lambda^2 - s}, \qquad s = GA^* - \rho I\omega^2 + Z_\theta \tag{17}$$

Substituting into Eq. (13), with $x = \lambda^2$, leaves a quadratic:

$$GA^*EI^*x^2 + [GA^*(GA^* - s) - pEI^*]x + ps = 0,$$
$$p = Z_x - \rho A\omega^2 \tag{18}$$

Two roots of the quadratic give the four exponents $\lambda_{1,2} = \pm\sqrt{x_1}$, $\lambda_{3,4} = \pm\sqrt{x_2}$ and four values of B_j from Eq. (17).

The particular solution is $w_p = a_1 \cos \kappa z$ for translation and $\theta_p = b_1 \sin \kappa z$ for rotation. Writing $\Delta = EI^*\kappa^2 + s$, the coefficients are:

ONLINE FIRST

$$D_p = -\frac{GA^*\kappa^2(\Delta - GA^*)}{\Delta} \tag{19}$$

$$a_1 = -\frac{Z_x}{D_p - p} \tag{20}$$

$$b_1 = -\frac{\kappa GA^* a_1}{\Delta} \tag{21}$$

The constant parts of Eq. (13), $-\cos\kappa L$ from u_{ff}^{rel} and the body force $\rho A\omega^2 u_b$ are combined to get the constant part of w:

$$W_c = -\cos\kappa L \tag{22}$$

Collecting the three parts, the general solution is obtained:

$$w(z) = \sum_{j=1}^{4} C_j e_j(z) + a_1 \cos\kappa z + W_c \tag{23}$$

$$\theta(z) = \sum_{j=1}^{4} C_j B_j e_j(z) + b_1 \sin\kappa z \tag{24}$$

$$M(z) = EI\left[\sum_{j=1}^{4} C_j B_j \lambda_j e_j(z) + b_1\kappa\cos\kappa z\right] \tag{25}$$

$$V(z) = -GA\left[\sum_{j=1}^{4} C_j(\lambda_j - B_j)e_j(z) - (a_1\kappa + b_1)\sin\kappa z\right] \tag{26}$$

The exponentials are written as:

$$e_j(z) = e^{\lambda_j\left(z - z_j^{ref}\right)}, \qquad z_j^{ref} = \begin{cases} L & Re\ \lambda_j > 0 \\ 0 & otherwise \end{cases} \tag{27}$$

in order to keep every term bounded by unity on $0 \le z \le L$.

Imposing the boundary conditions, Eq. (16), on Eqs. (23)–(26) and writing $e_j^0 = e_j(0)$ and $e_j^L = e_j(L)$ gives the system:

$$\begin{bmatrix} B_1\lambda_1 e_1^0 & B_2\lambda_2 e_2^0 & B_3\lambda_3 e_3^0 & B_4\lambda_4 e_4^0 \\ (\lambda_1 - B_1)e_1^0 & (\lambda_2 - B_2)e_2^0 & (\lambda_3 - B_3)e_3^0 & (\lambda_4 - B_4)e_4^0 \\ e_1^L & e_2^L & e_3^L & e_4^L \\ B_1 e_1^L & B_2 e_2^L & B_3 e_4^L & B_4 e_4^L \end{bmatrix} \begin{Bmatrix} C_1 \\ C_2 \\ C_3 \\ C_4 \end{Bmatrix} = \begin{Bmatrix} -b_1\kappa \\ 0 \\ (1 - a_1)\cos\kappa L \\ -b_1 \sin\kappa L \end{Bmatrix} \tag{28}$$

The rows, in order, correspond to the boundary conditions $M(0) = 0$, $V(0) = 0$, $w(L) = 0$ and $\theta(L) = 0$ for the fixed base. For the pinned base, the fourth row becomes $B_j\lambda_j e_j^L$ with $-b_1\kappa\cos\kappa L$ on the right-hand side.

The procedure of obtaining the closed-form solution is outlined hereafter. First, the acceleration record is zero-padded, transformed to the acceleration spectrum $S_a(\omega)$ by FFT, and converted to displacement:

$$U_{out}(\omega) = -\frac{S_a(\omega)}{\omega^2} \tag{29}$$

For each considered frequency bin ($f_{HP} < f \le f_{LP}$), κ and U_s follow from Eqs. (2) and (4). Spring impedances Z_x and Z_θ, as well as the coefficients p and s, can then be evaluated. Eq. (18) is solved for the four λ_j and Eq. (17) for the B_j. The system of equations (28) is solved for C_j. Response quantities are obtained by evaluating the Eqs. (23)–(26) at every depth and scaling by $U_s(\omega)$. An inverse FFT returns the time histories.

2.4 Model limitations and assumptions

The presented analytical formulation introduces certain simplifications, from which the real-world conditions often deviate, and which should be acknowledged in the course of the design process. The geological profile, as well as the soil-structure interface, are modeled as uniform along the shaft height. While sites with uniform and stable rock profiles are preferred for surge shaft placement, real-world conditions might include discontinuities, weathering zones, spatial variability of rock mass properties or unfavorable in-situ stress states. Each of the potential issues requires consideration beyond the scope of the idealized global analysis presented in this paper. Established solutions include empirical design decisions, local analyses, advanced finite-element modeling and iterative design process with parameters updated during the excavation, all beyond the scope of this paper.

3 Verification

3.1 Numerical model

Numerical analysis is conducted in two stages. In the first stage, free-field response under the ground motion is determined through one-dimensional elastic analysis in the frequency domain, using the Linear Elastic Calculator module of the Strata software package [16], specifically the pyStrata implementation [17]. Transfer functions are evaluated on pre-determined points along the profile height, which correspond to the structural finite-element model nodes. It should be noted that, for the given setup, the transfer-matrix solution of pyStrata algebraically reduces to the transfer function of the analytical solution. Despite it not being a mathematically independent verification, agreement of the free-field outputs is still useful to rule out gross errors in the analytical solution from Section 2.1. Transfer function, returned by pyStrata, is multiplied by the record's displacement spectrum to obtain the free-field displacement spectrum $U_{ff}(\omega)$ at each node depth. Base-relative displacement spectrum $U_{ff}^{rel}(\omega)$ is derived by subtracting the absolute displacement spectrum at $z = L$. Velocity and acceleration are calculated in the frequency domain by multiplying $U_{ff}^{rel}(\omega)$ with $i\omega$ and $-\omega^2$, respectively. Time histories of displacements, velocities and accelerations are generated by inverse FFT of the spectra.

In the second stage, an elastic finite-element (FE) model is established and analyzed in the time domain, using the OpenSeesPy implementation [18] of the OpenSees computational framework [19], as schematically presented in Fig. 3. The surge shaft is modeled as a series of finite elements with Timoshenko beam formulation, laterally and rotationally supported by a series of discrete springs at every node, while the base is fixed or pinned. As in the analytical model, the effective shear area of the annular cross section is adopted according to Cowper [14]. Stiffness-proportional Rayleigh damping is applied to the beam elements, using the same β_K as the analytical model. Springs and dashpots are calibrated consistently with the analytical model, Eqs. (11)–(12), only scaled by tributary length at each node, equal to the finite element size. Free-field displacement, velocity and acceleration histories are applied at the far ends of the

ONLINE FIRST

springs (i.e. the ends not connected to the shaft) using a multi-support excitation pattern in OpenSees. Far ends of the springs are rotationally restrained, so $\varphi_{ff} = 0$ is enforced. Inertia from absolute base acceleration is applied as a series of forces directly onto the shaft nodes. At each node i, the inertial force is defined as:

$$F_i(t) = -m_i \cdot \ddot{u}_b(t) \tag{30}$$

where m_i is the tributary structural mass. Newmark integration scheme (γ=0.5, β=0.25) with four sub-steps per record step is used. At each step, nodal translations and rotations, as well as the element forces, are recorded. Bending moments and shear forces are averaged at nodes. The end moments and shear forces, at $z = 0$ and $z = L$, are corrected to account for the lumped boundary effects of the FE model.

It should be noted that Fig. 3 shows the OpenSees coordinate system convention. For consistency, all the results are presented using the downward z-axis convention, as in Fig. 2.

3.2 Setup

The following benchmark case is considered. The surge shaft is 60 m deep, with a constant cross-section with 12 m external diameter and 1.2 m wall thickness. Elastic modulus, density and Poisson's ratio of reinforced concrete are taken as 33 GPa, 2500 kg/m^3 and 0.2, respectively.

The site is defined as a 60 m deep homogeneous layer of weathered rock, sitting on top of an intact rock half-space. Properties of the layer and of the half-space are listed in Table 1.

Table 1. Rock properties at the considered site

Parameter	Value	Note
Weathered rock layer		
E_s [GPa]	1.6	Rock mass modulus
ρ_s [kg/m^3]	2400	Density
v_s	0.25	Poisson's ratio
ξ_s	0.05	Damping ratio
Intact rock half-space		
V_r [m/s]	1200	Shear wave velocity
ρ_r [kg/m^3]	2600	Density
ξ_r	0.01	Damping ratio

Structural damping of the lining is stiffness-proportional Rayleigh, with β_K calibrated to 5% at the soil layer's first natural resonance frequency [12]:

$$f_1 = \frac{V_s}{4L} \tag{31}$$

which is equal to 2.15 Hz. Winkler spring and dashpot coefficients returned by Eqs. (11) and (12) are listed in Table 2.

Table 2. Values of coefficients of Winkler springs and dashpots

Parameter	Value	Unit
k_x	$2.27 \cdot 10^9$	N/m per m of depth
k_θ	$7.24 \cdot 10^{10}$	N·m/rad per m of depth
c_x	$5.71 \cdot 10^7$	N·s/m per m of depth

Note that the k_x from Gerolymos and Gazetas [8] is equal to 1.42E_s, which is on the conservative side of 1.2E_s, commonly assumed for piles, and used by Zhang et al. [5] for shaft analysis.

The base is assumed to be fixed. The numerical model is discretized into 30 finite elements along the shaft height. Load case with the empty surge shaft was taken as a baseline.

The applied ground motion is the 90° component of Kobe (1995), recorded at the Kobe University (KBU) station, which is a natural rock outcrop motion. High-pass filter at 0.05 Hz is applied to prevent the low-frequency noise from introducing baseline drift through integration. A low-pass filter with a cutoff frequency of 12 Hz is applied, due to the limits of the spring and dashpot calibration. Besides that, 95% of the ground motion's energy content sits below 8 Hz, as shown in Fig. 4.

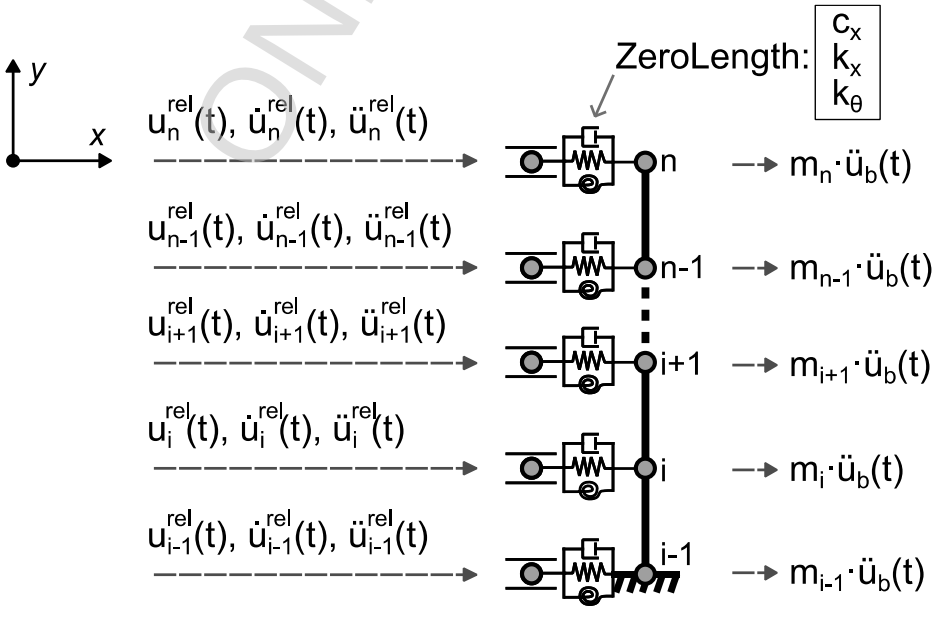


Figure 3. The numerical OpenSees model

ONLINE FIRST

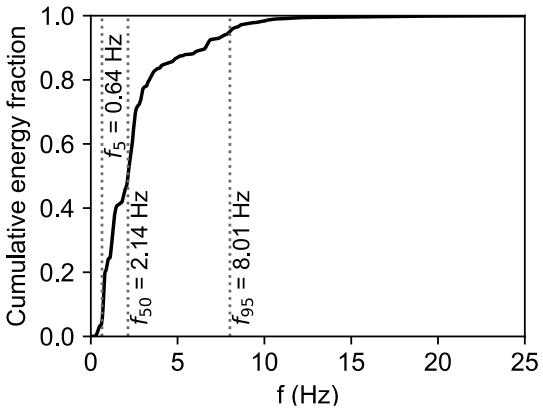


Figure 4. Cumulative energy plot of the KBU-90 record

3.3 Results

The first check, independent of ground motion, is done by comparing the natural frequencies of analytical and numerical shaft models. The first four frequencies of both models are listed in Table 3.

Table 3. Comparison of natural frequencies of analytical and FE model

Mode	f_i [Hz] analytical	f_i [Hz] numerical	Diff. [%]
1	24.034	24.034	-0.001
2	26.915	26.907	-0.030
3	35.150	35.103	-0.136
4	47.271	47.116	-0.327

Time histories of the shaft response, recorded at the depth of 20 m, are plotted in Fig. 5. The plot is cropped at 20 s for readability.

Envelopes of shaft displacements, rotations, bending moments and shear forces obtained from both models are presented in Fig. 6.

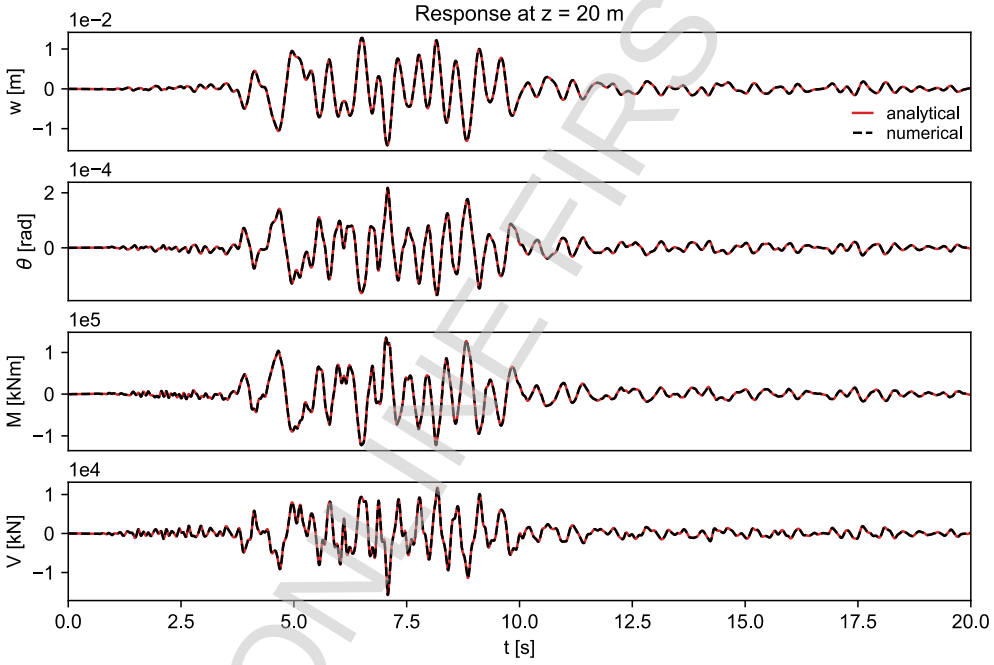


Figure 5. Shaft response histories at the depth of 20 m, analytical vs. numerical solution

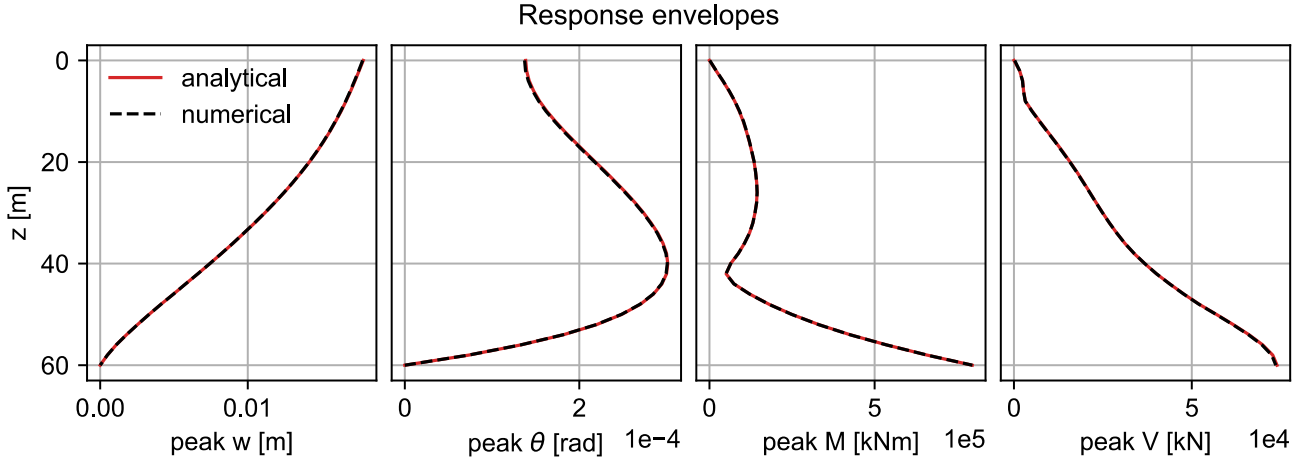


Figure 6. Shaft response envelopes: analytical vs. numerical solution

ONLINE FIRST

Peak values of each response parameter from Fig. 6 are listed in Table 4.

Table 4. Peak values of response quantities: analytical vs. numerical solution

Quantity	Peak analytical	Peak numerical	Diff. [%]
w [m]	0.01783	0.01779	-0.219
θ [rad]	3.014e-4	3.008e-4	-0.184
M [kNm]	7.953e5	7.958e5	0.056
V [kN]	73941	73590	-0.474

The results indicate a nearly exact agreement between the analytical solution presented in Section 2 and the independent time-domain numerical solution of the same problem, described in Section 3.1. The differences of peak response quantities, listed in Table 4, are consistent with discretization error of the FE model. The intended functionality and accuracy of the proposed frequency-domain closed-form solution are therefore confirmed.

4 Parametric study

The parametric study was conducted by varying the input parameters of the analytical model presented in Section 2. The set of input parameters, outlined in Section 3.2, was used as a baseline. The results are reported in terms of envelopes of response quantities.

4.1 Beam formulation

In Fig. 7, envelopes of the response quantities are compared for Euler-Bernoulli and Timoshenko beam formulations. Euler-Bernoulli beam was simulated by multiplying the shear area with 10^3 in the same analytical framework presented in Section 2.

It is obvious that the considered structural proportions warrant the consideration of shear deformability. For the analysis of surge shafts specifically, no benefit of the Euler-Bernoulli beam formulation can be established. Timoshenko beam with the effective shear area adopted according to Cowper [14] is found to provide plausible results. As Kampitsis et al. [20] point out, Timoshenko beam theory provides better accuracy in pile models as well. Timoshenko beam formulation is also used for longitudinal response analysis of tunnels [21].

4.2 Base fixity

To avoid complex, potentially unreliable and case-dependent FE-based calibration of a rotational spring at the shaft base, two boundary cases were considered: fixed and pinned. Response envelopes for both cases are presented in Fig. 8.

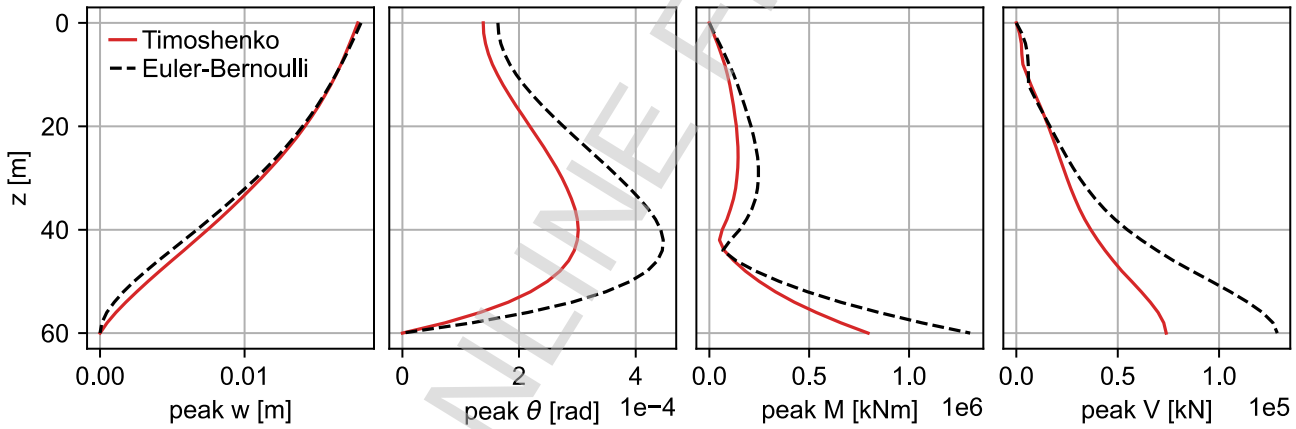


Figure 7. Shaft response envelopes: Influence of assumed beam kinematics

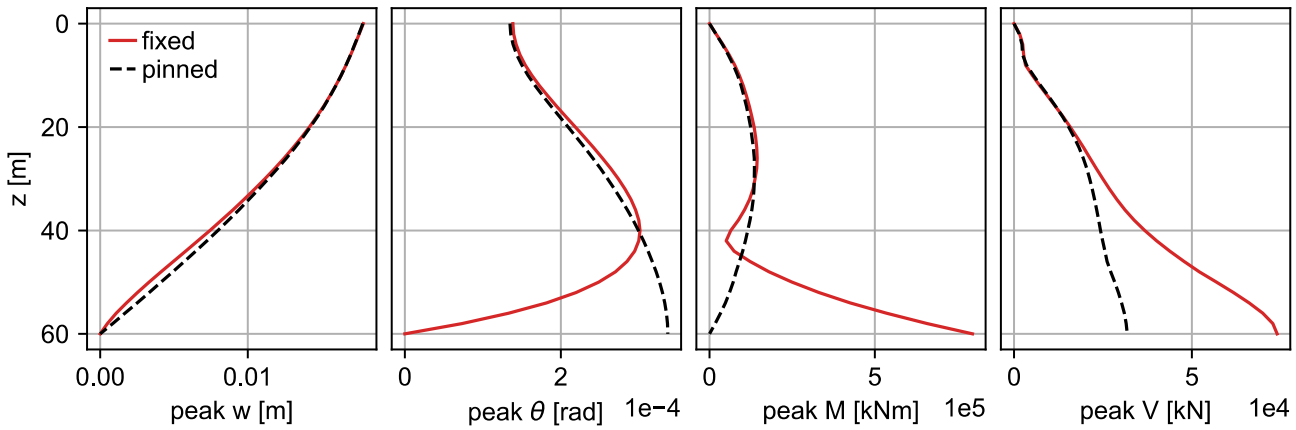


Figure 8. Shaft response envelopes: Effect of base BC

ONLINE FIRST

As can be observed from Fig. 8, fixed base provides an upper-bound estimate of section forces at the lower segment of the shaft, while the response envelopes on the upper parts remain mostly unaffected. Values of moment and shear force, obtained with the fixed-base idealization, are of the expected order of magnitude, and are usable for design checks. Therefore, for the considered configuration, the fixed-base boundary condition may be adopted as a safe engineering approximation and used for design purposes. It should be noted that a different structural layout – e.g. if there are adjacent structures that interact with the surge shaft – might warrant a different treatment of the boundary conditions.

4.3 Lateral spring stiffness

Consequences of translational Winkler spring calibration were investigated by conducting a sensitivity sweep with 50, 100 and 150% of the k_x value given by Eq. (11). The response envelopes are presented in Fig. 9.

Taking the full k_x value for reference, it can be concluded that the k_x reduction of 50% reduces the peak shear force, recorded at the base, by 12.5%. Spring stiffness increase to 150% of the reference value increases the peak shear force by 8.5%. Peak shear force asymptotically reaches the upper bound of ~$1.5 \cdot 10^5$ kN as the spring stiffness approaches infinity, as presented in Fig. 10. Uncertainty may be mitigated by conducting sensitivity checks. The bending moments also asymptotically converge, albeit with a smaller overall sensitivity to k_x.

4.4 Influence of rotational springs

Two boundary cases in terms of rotational soil-structure compliance were analyzed: rotational springs as per Eq. (11), and unrestrained rotation of the shaft. The envelopes are plotted in Fig. 11.

As expected, the assumption of perfect shear bond around the lining envelope tends to increase the shear demand. For design purposes, an envelope of both cases may be considered, since the model with no rotational springs produces slightly larger bending moments and top displacement.

Actual interface conditions, where a partial shear interaction is expected to develop, should be sitting between the two idealized boundary cases. Exact degree of shear transfer and possible cyclic degradation of the bond are influenced by excavation and construction technology, as well as by time-dependent phenomena. The analysis was thus simplified, so to avoid uncertain and time-dependent input parameters.

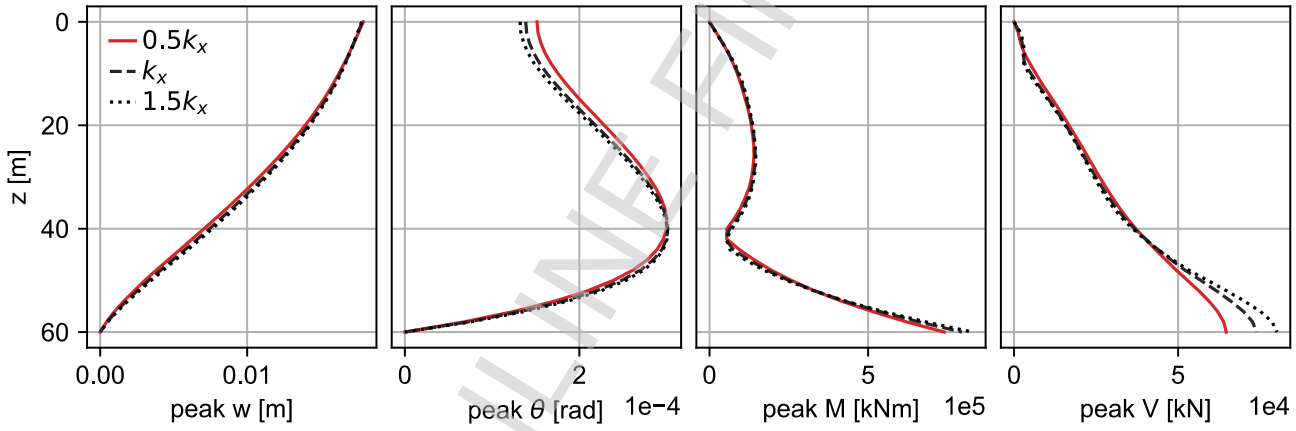


Figure 9. Shaft response envelopes: Lateral Winkler springs sensitivity sweep

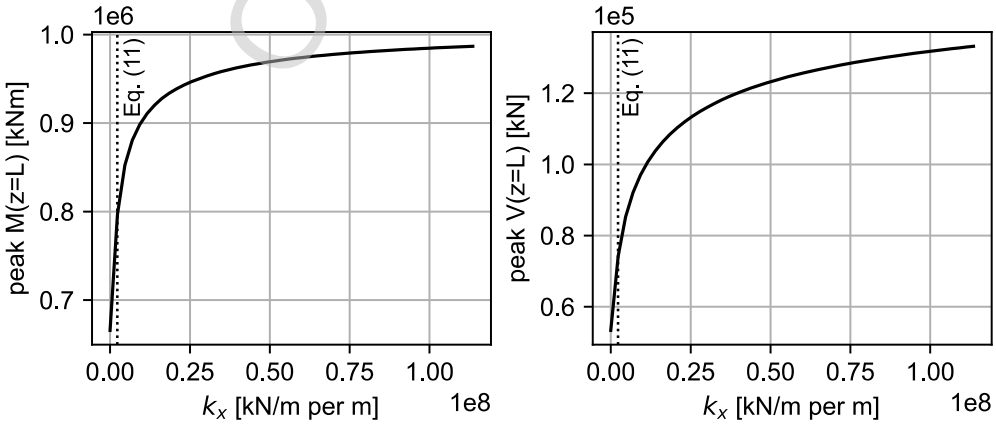


Figure 10. Dependence of peak moment and shear force on lateral spring stiffness

ONLINE FIRST

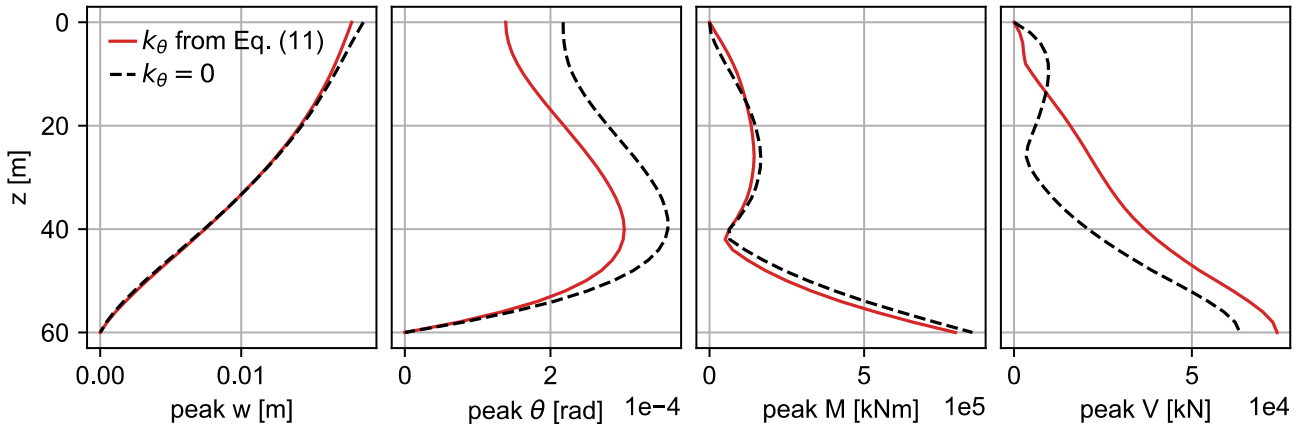


Figure 11. Shaft response envelopes: Effect of rotational Winkler springs

4.5 Influence of shaft inertia

Three cases were considered:

- Surge shaft filled with water. Lining mass and the impulsive mass of water were taken into account by adopting an equivalent lining density ρ, with the convective inertia assumed to be negligible.
- Empty surge shaft with the lining mass modeled.
- A model with no structural mass.

The envelopes are presented in Fig. 12.

The results, Fig. 12, indicate that the conservative estimate of mass, where the surge shaft is assumed to be filled to the top, results in shear force increase of 4.3% at the base, with other response parameters mostly unaffected.

4.6 Radiation damping

In terms of radiation damping of the surrounding rock, two boundary cases were considered: Lateral dashpots calibrated according to the high-frequency asymptote of Gazetas and Dobry [15], and no radiation damping, i.e. $c_x = 0$.

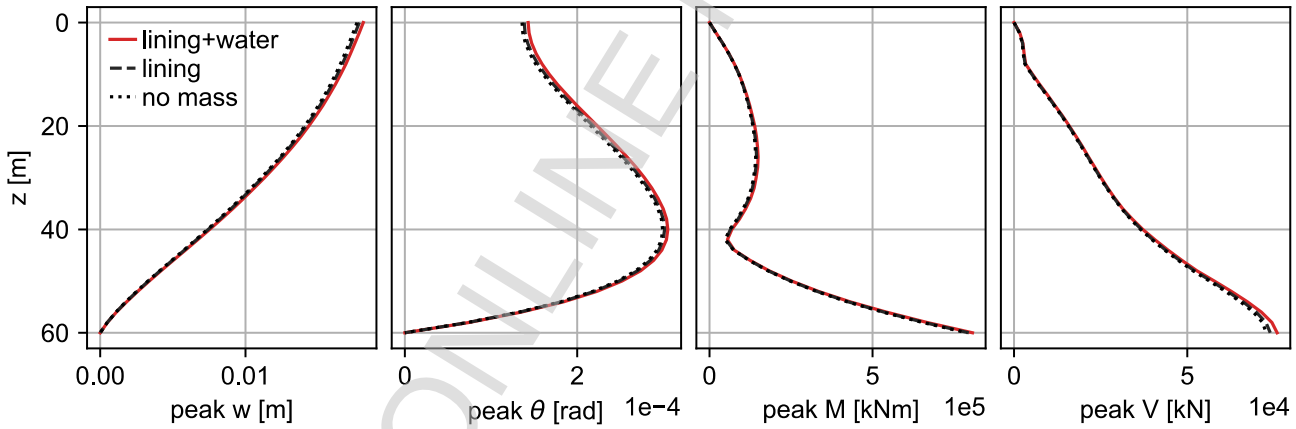


Figure 12. Shaft response envelopes: Influence of shaft and water inertia

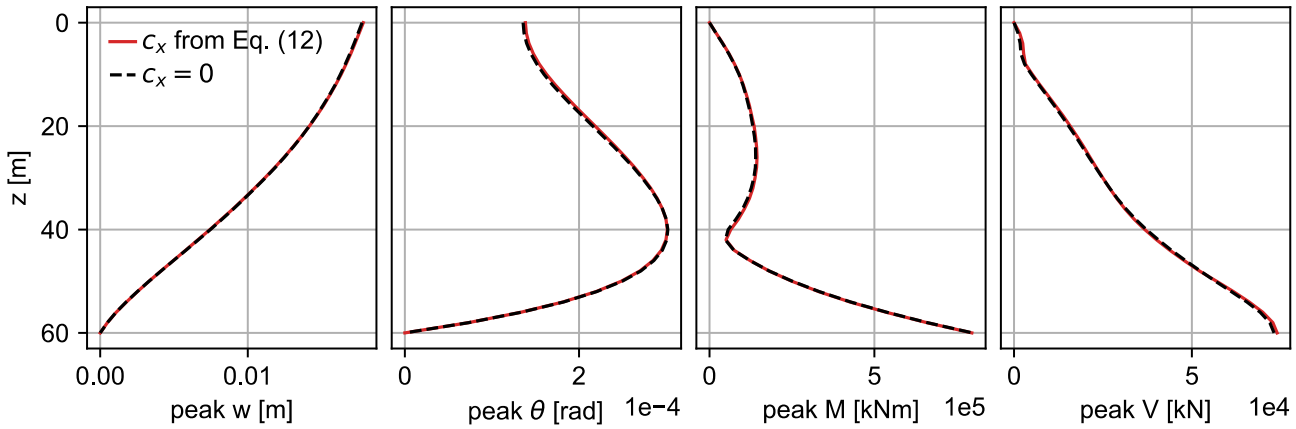


Figure 13. Shaft response envelopes: Influence of radiation damping

ONLINE FIRST

As can be observed from Fig. 13, influence of the lateral dashpots may be considered negligible. In the considered case, the kinematic coupling through dashpots increases the peak shear force by 1.2% at the base, with some minor increase near the surface as well. The other response quantities remain unaffected. Hence, the dashpot calibration is practically inconsequential in the considered scenario. The results are consistent with the formulation of the complex impedance Z_x, which has a dual role: energy dissipation and kinematic coupling. The dashpots are retained in the model mostly for future extensibility.

5 Conclusions

A closed-form frequency-domain solution for seismic analysis of surge shafts was presented and evaluated in this paper. Verification has confirmed the proposed solution's consistency with independent numerical results. Results of the conducted analyses indicate that, for the considered configuration (RC-lined surge shaft in rock), the response is predominantly governed by kinematic compliance with the surrounding ground, rather than by dynamic effects. The proposed analytical solution, along with the provided benchmark case, is primarily intended for preliminary analyses and baseline verification of more advanced numerical models. The following analysis decisions, intended to mitigate or eliminate the modeling uncertainties, are recommended on the basis of the conducted parametric study:

- Base boundary conditions: Model the shaft base as fixed, as that idealization provides upper-bound response envelopes for the considered configuration.
- Lateral spring calibration: Conduct a sweep in reasonable boundaries to mitigate uncertainties, both in terms of geological data and spring calibration.
- Rotational springs: Analyze both with and without rotational interaction and take worst-case results.
- Structural mass: Analyze the load case with water-filled shaft.

Following the presented points, analysis results for each ground motion should be taken as an envelope of a minimum of four separate cases in terms of Winkler springs calibration:

- Lower-bound k_x and $k_\theta = 0$;
- Lower-bound k_x and k_θ from Eq. (11);
- Upper-bound k_x and $k_\theta = 0$;
- Upper-bound k_x and k_θ from Eq. (11).

The presented conclusions and recommendations were derived for a particular geological profile and structural layout, which is intended to represent a typical surge shaft design scenario. Hence, the presented procedure should be applicable in the majority of cases, at least in the preliminary phase. It is noted that a different geological profile (soft soil or multiple layers) or a different structural layout might warrant a modification to the current approach.

Future research is planned to extend in two directions:

- Simplified nonlinear analysis of surge shafts, based on the OpenSees numerical model introduced in this paper. Material nonlinearity of the shaft lining is to be introduced by using distributed-plasticity finite elements with fiber sections. At this point, it is hypothesized that consideration of moment redistribution might enhance the accuracy of stress state prediction, which is relevant for both capacity and serviceability checks. An appropriate shear behavior needs to be assigned to the lining as well.
- A series of continuum-based FE analyses, in order to further investigate the modeling assumptions, as well as to gain insight into stress-strain states around openings and near the base. Optimized structural detailing of the critical zones is to be proposed based on the results.

CRediT authorship contribution statement

BS: Conceptualization, Investigation, Methodology, Software, Validation, Writing – Review & Editing. NT: Data curation, Investigation, Methodology, Software, Visualization, Writing – Original Draft.

Conflict of interest

The authors declare no conflict of interest.

Acknowledgements

This work was financially supported by the Ministry of Science, Technological Development and Innovation of the Republic of Serbia under the Contract No. 451-03-33/2026-03/200012.

Data availability

Verification code is available at Zenodo (DOI: 10.5281/zenodo.22172571).

Ground motion data were obtained from the Center for Engineering Strong Motion Data (CESMD; https://www.strongmotioncenter.org).

References

[1] C.M. St John, T.F. Zahrah, Aseismic design of underground structures, Tunn. Undergr. Space Technol. 2 (1987) 165–197. https://doi.org/10.1016/0886-7798(87)90011-3.

[2] Y.M.A. Hashash, J.J. Hook, B. Schmidt, J. I-Chiang Yao, Seismic design and analysis of underground structures, Tunn. Undergr. Space Technol. 16 (2001) 247–293. https://doi.org/10.1016/S0886-7798(01)00051-7.

[3] G. Anoyatis, R. Di Laora, A. Mandolini, G. Mylonakis, Kinematic response of single piles for different boundary conditions: Analytical solutions and normalization schemes, Soil Dyn. Earthq. Eng. 44 (2013) 183–195. https://doi.org/10.1016/j.soildyn.2012.09.011.

[4] B. Zhang, Z.Y. Chen, General Winkler Model for Kinematic Responses of Shafts in Linear Soil, Int. J. Comput. Methods 17 (2020) 1940004. https://doi.org/10.1142/S0219876219400048.

[5] B. Zhang, L. Lu, Z. Zhong, X. Du, M.H. El Naggar, Analytical solution for seismic response of vertical shaft with primary and secondary linings under SH wave excitation, Comput. Geotech. 164 (2023) 105813. https://doi.org/10.1016/j.compgeo.2023.105813.

[6] J. Yang, H. Di, X. Zhang, C. He, S. Zhou, Analytical solution for kinematic response of double-lined shafts in unsaturated soil under vertically propagating SH-waves, Appl. Math. Model. 152 (2026) 116616. https://doi.org/10.1016/j.apm.2025.116616.

[7] Varun, D. Assimaki, G. Gazetas, A simplified model for lateral response of large diameter caisson foundations—Linear elastic formulation, Soil Dyn. Earthq. Eng. 29 (2009) 268–291. https://doi.org/10.1016/j.soildyn.2008.02.001.

[8] N. Gerolymos, G. Gazetas, Winkler model for lateral response of rigid caisson foundations in linear soil, Soil Dyn. Earthq. Eng. 26 (2006) 347–361. https://doi.org/10.1016/j.soildyn.2005.12.003.

ONLINE FIRST

[9] N. Gerolymos, G. Gazetas, Development of Winkler model for static and dynamic response of caisson foundations with soil and interface nonlinearities, Soil Dyn. Earthq. Eng. 26 (2006) 363–376. https://doi.org/10.1016/j.soildyn.2005.12.002.

[10] Y.O. Beredugo, M. Novak, Coupled Horizontal and Rocking Vibration of Embedded Footings, Can. Geotech. J. 9 (1972) 477–497. https://doi.org/10.1139/t72-046.

[11] N. Tomić, B. Stupar, Winkler modeling of vertical shafts in rock under vertically propagating shear waves: Verification code, (2026). https://doi.org/10.5281/zenodo.22172571.

[12] S.L. Kramer, Geotechnical Earthquake Engineering, Prentice Hall, New Jersey, USA, 1996.

[13] L. Dormieux, J. Canou, Determination of dynamic characteristics of a soil based on a cyclic pressuremeter test, in: Proceedings of the Third International Symposium on Pressuremeters, organised by the British Geotechnical Society and held at Oxford University, 2–6 April 1990, Emerald Publishing Limited, 1990, pp. 159–168. https://doi.org/10.1680/p3is.15562.0015.

[14] G.R. Cowper, The Shear Coefficient in Timoshenko's Beam Theory, J. Appl. Mech. 33 (1966) 335–340. https://doi.org/10.1115/1.3625046.

[15] G. Gazetas, R. Dobry, Simple Radiation Damping Model for Piles and Footings, J. Eng. Mech. 110 (1984) 937–956. https://doi.org/10.1061/(ASCE)0733-9399(1984)110:6(937).

[16] A.R. Kottke, E.M. Rathje, Technical manual for Strata, Pacific Earthquake Engineering Research Center, University of California, Berkeley, 2008.

[17] A. Kottke, M. Millen, S. Bot, subsurfaceiodev, arkottke/pystrata: v0.5.4, (2024). https://doi.org/10.5281/zenodo.11130778.

[18] M. Zhu, F. McKenna, M.H. Scott, OpenSeesPy: Python library for the OpenSees finite element framework, SoftwareX 7 (2018) 6–11. https://doi.org/10.1016/j.softx.2017.10.009.

[19] F. McKenna, M.H. Scott, G.L. Fenves, Nonlinear Finite-Element Analysis Software Architecture Using Object Composition, J. Comput. Civ. Eng. 24 (2010) 95–107. https://doi.org/10.1061/(ASCE)CP.1943-5487.0000002.

[20] A.E. Kampitsis, E.J. Sapountzakis, S.K. Giannakos, N.A. Gerolymos, Seismic soil–pile–structure kinematic and inertial interaction—A new beam approach, Soil Dyn. Earthq. Eng. 55 (2013) 211–224. https://doi.org/10.1016/j.soildyn.2013.09.023.

[21] A.L. Sánchez-Merino, J. Fernández-Sáez, C. Navarro, Simplified longitudinal seismic response of tunnels linings subjected to surface waves, Soil Dyn. Earthq. Eng. 29 (2009) 579–582. https://doi.org/10.1016/j.soildyn.2008.06.003.

ONLINE FIRST